

ARMY RESEARCH LABORATORY



# RCS Validation of a Missile-Shaped Target at W-Band

by Geoffrey H. Goldman

ARL-TR-1563

January 1998

19980210 092

DTIC QUALITY INSPECTED 3

Approved for public release; distribution unlimited.

The findings in this report are not to be construed as an official Department of the Army position unless so designated by other authorized documents.

Citation of manufacturer's or trade names does not constitute an official endorsement or approval of the use thereof.

Destroy this report when it is no longer needed. Do not return it to the originator.

---

## Abstract

---

In a comparison of measured, simulated, and theoretical calculations of radar cross section (RCS), the radar target was a simple missile shape (a cylinder with hemispherical ends). For the measurements, the target was rotated on a turntable from  $-5^\circ$  to  $365^\circ$  in azimuth, and its RCS was measured with a W-band frequency-agile instrumentation radar. (Clutter and noise in the measured RCS data were reduced by spatial filtering.) For modeling the target geometry, the ACAD (advanced computer-aided design) geometric modeling program was used to create both an IGES (initial graphics exchange specification) and a facet model. For modeling the RCS, three high-frequency prediction codes were used (Xpatch, CADDSCAT, and NcPTD), as well as a point scatter model. Various methods were used to process and simulate the target returns, depending upon the aspect angle. Agreement between the measured and simulated bandwidth-averaged RCS values depended on the portion of the target that dominated the radar return: agreement was close for radar returns dominated by returns from the hemispherical ends of the target. However, for aspect angles near broadside to the target (for which the cylindrical part of the target dominated the returns), RCS measurements suggested an interaction between the target and the pylons supporting it.

## Contents

<b>1. Introduction .....</b>	<b>1</b>
<b>2. Modeling and Experimental Setup .....</b>	<b>2</b>
2.1 <i>Target Characteristics</i> .....	2
2.2 <i>Target Model</i> .....	3
2.3 <i>Radar Characteristics</i> .....	4
2.4 <i>Measured Data</i> .....	4
2.5 <i>Simulation Models</i> .....	5
<b>3. Procedure .....</b>	<b>8</b>
3.1 <i>Processing</i> .....	8
3.1.1 <i>Get Data</i> .....	8
3.1.2 <i>Filter</i> .....	8
3.1.3 <i>Image</i> .....	10
3.1.4 <i>Extract</i> .....	10
3.1.5 <i>Inverse</i> .....	12
3.1.6 <i>Bandwidth Average</i> .....	12
3.2 <i>Antenna Pattern</i> .....	13
3.3 <i>Parameters</i> .....	13
<b>4. Results .....</b>	<b>16</b>
4.1 <i>Theory and Near-Field Model</i> .....	16
4.2 <i>Comparison of Simulation, Theory, and Measurement</i> .....	17
4.2.1 <i>Hemispheres</i> .....	17
4.2.2 <i>Cylinder</i> .....	19
<b>5. Conclusion .....</b>	<b>25</b>
<b>Acknowledgments .....</b>	<b>26</b>
<b>References .....</b>	<b>27</b>
<b>Distribution .....</b>	<b>29</b>
<b>Report Documentation Page .....</b>	<b>33</b>

## Figures

1. Test target and pylons on turntable .....	2
2. Geometry of test target at 0° azimuth angle .....	3
3. Geometric target model represented by IGES 128 surface patches .....	4
4. RCS for a 22.5° dihedral averaged over 2000 measurements .....	6
5. Phase variation for a 22.5° dihedral averaged over 2000 measurements .....	6
6. Signal flow diagram of data processing .....	8
7. Flow chart for computing bandwidth-averaged RCS .....	9
8. ISAR image of target for region dominated by a hemisphere .....	11
9. ISAR image of target for region dominated by cylinder .....	11
10. Two-way azimuth angle antenna pattern for VV polarization .....	13
11. Bandwidth-averaged RCS unprocessed and processed with 128-ramp ISAR technique .....	14

12. Bandwidth-averaged RCS smoothed with a 144-point moving-average filter .....	15
13. Bandwidth-averaged RCS values for measured data and a point scatter model .....	18
14. Bandwidth-averaged RCS values for Xpatch and CADDSCAT simulation .....	18
15. Bandwidth-averaged and single-frequency RCS for measured data .....	20
16. RCS calculated with CADDSCAT for different phase delays .....	21
17. RCS calculated with NcPDT for different phase delays .....	21
18. RCS calculated with CADDSCAT and measured RCS processed with antenna pattern corrections .....	22
19. RCS calculated with NcPDT and measured RCS processed without antenna pattern corrections .....	22

## Tables

1. Radar characteristics at W-band .....	5
2. Standard deviation of RCS and phase variation of 22.5° dihedral calculated over frequencies that have a high SNR .....	7
3. Standard deviation calculated for low-noise region dominated by returns from hemispheres .....	15
4. Measured and simulated RCS values for returns dominated by a hemisphere .....	18
5. Crossover angles and RCS statistics .....	23
6. Mean and standard deviation of RCS and energy density spectrum statistics for data with nulls removed .....	23

# 1. Introduction

The proliferation of tactical ballistic missiles throughout the world has provided motivation for the United States to develop theater ballistic missile defense systems such as Patriot, Theater High-Altitude Air Defense (THAAD), Navy Area, Navy Theater Wide, and Medium-Extended Air Defense System (MEADS). Previously developed missiles using conventional fuzing systems have difficulty destroying fast-moving "Scud-like" missiles. To defeat targets with high speed and/or agility and intensive countermeasures, new missiles are being developed that use techniques such as hit-to-kill or guidance integrated fuzing (GIF). Because of the high cost of field testing, computer simulations will have a significant role in the development of these systems.

Important to such computer simulations are validated and computationally efficient radar backscatter target models. There are several validated radar cross section (RCS) predictive codes, but their levels of validation depend upon target, frequency, range, and computer processing time [1]. Several codes perform well when used for a specific application, but no code has been found that is computationally efficient and can model all the features desired for simulating GIF for complex targets (these include multi-bounce effects, near-field effects, variable antenna patterns, multiple targets, and traveling waves). This report compares measured, simulated, and theoretical calculations of bandwidth-averaged RCS for a missile-shaped target at W-band.

The Army Research Laboratory (ARL) measured the radar backscatter of a test target consisting of a cylinder capped by two hemispheres, as the target rotated on a turntable. Measurements were made at Aberdeen Proving Ground with a frequency-agile, coherent, polarimetric, instrumentation radar built by ARL. The measurements were made in the far field of the target, except for aspect angles near broadside to the cylindrical portion of the target. Although the full linear polarization scattering matrix was measured, this report analyzes only the vertical-transmit, vertical-receive (VV) polarization.

The radar returns were simulated with three mature high-frequency RCS prediction codes\* (Xpatch [2], CADDSCAT [3], and NcPDT [4]) and a point scatter model (PSM). These codes use physical optics (PO) and the physical theory of diffraction to calculate electric fields and RCS [5]. They cannot simulate traveling or creeping waves.

Techniques were developed to reduce and separate the noise and clutter from the target signature. To enable a direct comparison between measured data and simulated results, I processed the measured data with spatial filters that reduced clutter, noise, and (if present) traveling and creeping waves. For most aspect angles, the scattering due to traveling and creeping waves and noise appeared to be negligible. The RCS at aspect angles where such scattering may have been significant was calculated, but not analyzed.

---

\*Xpatch and NcPDT are a product of DEMACO, and CADDSCAT is a product of Boeing/McDonnell-Douglas. The federal government has contributed to the development of these codes through the Electromagnetic Code Consortium.

## 2. Modeling and Experimental Setup

### 2.1 Target Characteristics

The test target was a cylinder with hemispherical ends, as pictured in figure 1. The cylinder is made up of three sections, which were threaded at the ends so that they could be screwed together. The cylinder is 180 in. long, with each section being 60 in. long. The radius of the hemispheres is 4 in., so that the diameter of the cylinder is 8 in. The hemispheres are also threaded so that they can be screwed onto the ends of the cylinder, and there is a 3/8-in. extension on each hemisphere for the threads. The gaps between the seams of the cylinder were all less than 0.002 in. The overall length of the test target is 188.75 in.: 180 in. for the cylinder, 4 in. for each hemisphere, and 0.375 in. for a cylindrical extension on each hemisphere. The approximate weight of the target is 400 lb. (Fig. 3, sect. 2, illustrates the dimensions of the target.)

The target was supported by two buoyant Styrofoam pylons that were shaped to have a minimum RCS at aspect angles near  $0^\circ$  azimuth. The width of the top of the pylons (shown in fig. 1) was approximately 1/8 to 1/4 of an inch, and increased to approximately 1.5 in. at the bottom of the test target. These widths are important, because a radar signal would be slightly delayed while propagating through the pylons towards a target for certain aspect angles. The exact dimensions of the pylons were difficult to measure and quantify because they are curved three-dimensional (3-D) objects.

During the measurements, the target was placed 30 in. from the center of rotation of the turntable, with  $0^\circ$  azimuth angle, corresponding to the geometry shown in figure 2. The depression angle was  $1.45^\circ$  with respect to the radar (a positive depression angle implies that the radar was above the target). The peak of the antenna pattern was pointed towards the target at

Figure 1. Test target and pylons on turntable (aspect angle near broadside).

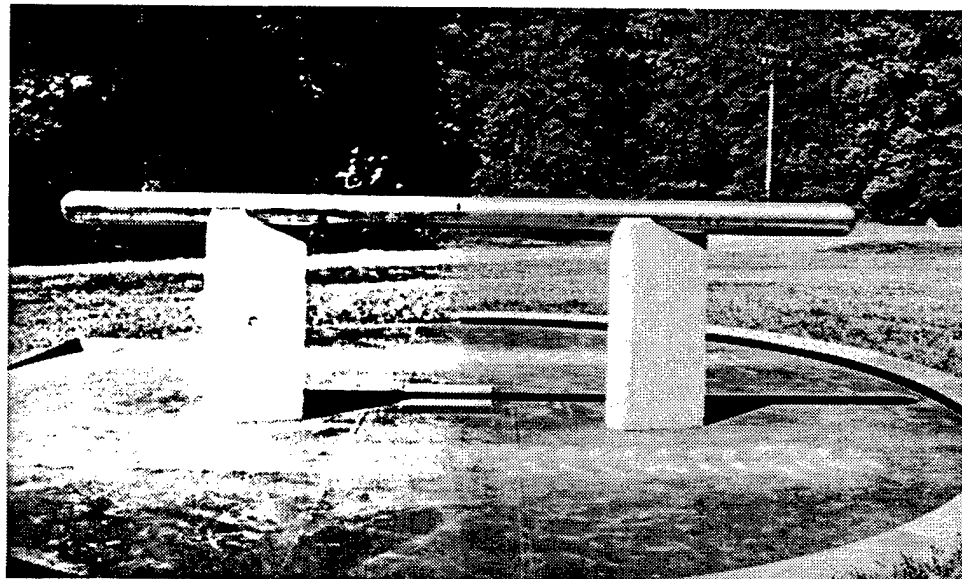
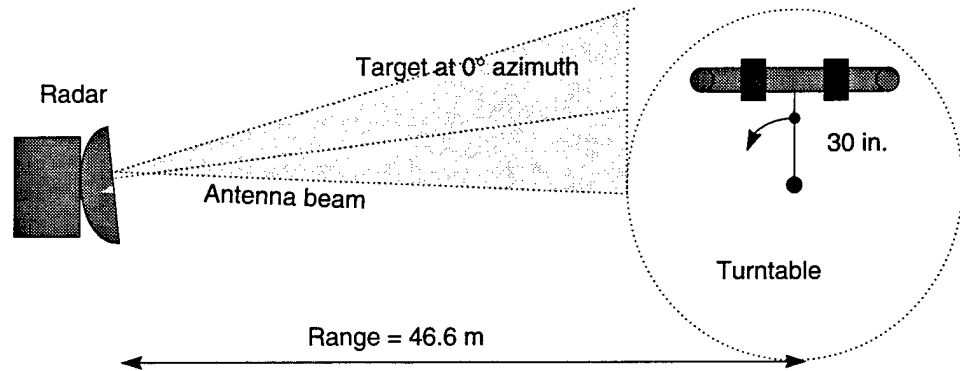


Figure 2. Geometry of test target at 0° azimuth angle.



0° azimuth angle. The two-way, 3-dB width of the antenna pattern was approximately 4.4°, which was slightly smaller than the target at broadside at a range of 46.6 m. The exact location of the target and the antenna pattern were determined through a Monte Carlo simulation based upon the radar measurements.

## 2.2 Target Model

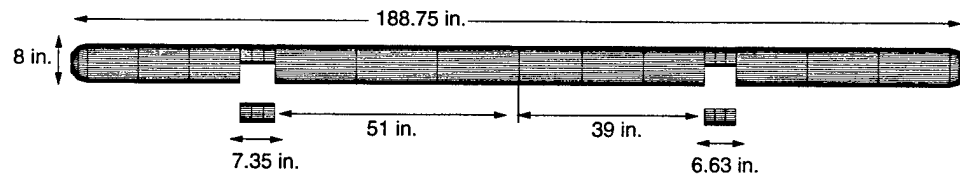
For input to the NcPDT, CADDSCAT, and Xpatch simulation codes, I generated the test target surface using the ACAD (advanced computer-aided design) software program. All the simulation codes could handle multiple geometric representations; I chose two commonly used representations for the target model: an IGES (initial graphics exchange specification) format and a facet model format. I created arbitrary surface patches by revolving lines and curves; to determine the number of surface patches to use, I increased the number of patches until the RCS converged to a constant for the hemisphere portion of the target. (This approach is based on the fact that the RCS of a sphere, in the far field, is constant and independent of aspect angle at high frequencies.) I calculated the standard deviation of bandwidth-averaged RCS simulated with CADDSCAT at different aspect angles and compared these values to a threshold. I then increased the number of surface patches in the IGES representation until the standard deviation of the simulated RCS was less than or equal to 0.1 dB. This resulted in a model for the hemispheres that contained 18 spherical slices of 20°.

I followed a similar procedure for Xpatch, using the same ACAD model, but with the facet model representation. For CADDSCAT, I implemented a rectangular gap model using spline representations of the gaps created by the physically segmented target.

The cylinder section of the target was modeled with six smaller cylinders as shown in figure 3. The lengths of the cylinders were determined by the starting and ending horizontal position of the top of the pylons. The four larger cylinders each contained 18 cylindrical slices of 20°. The two smaller cylinders contained 16 cylindrical slices of 20° and 4 of 10°. These smaller cylinders were divided into top and bottom sections. (In the figure, the bottom cylinders are offset from the top cylinders for visual clarity.) The length of the bottom sections corresponded to the measured length of the



**Figure 3. Geometric target model represented by IGES 128 surface patches. Smaller half cylinders at bottom are offset from main target for clarity.**



Styrofoam columns supporting the target (and obscuring parts of it); the height of the half cylinder was set to 4 in., the position of specular reflection for a radar at a  $0^\circ$  depression angle. However, the measurements indicated that on the actual target, this height varied slightly from 4 in. Since the simulated RCS was very sensitive to the pylon vertical location for values near 4 in., the inability to input the true dimension affected the model results. Figure 3 shows the ACAD model of the test target.

For diagnostic purposes, a PSM was constructed to simulate the returns from the hemispheres. The model consisted of a single scatterer with a constant amplitude, with a position that tracked the specular reflection point for the appropriate hemisphere.

## 2.3 Radar Characteristics

ARL has a coherent fully polarimetric radar system capable of operation at X-band,  $K_a$ -band, or W-band [6]. Table 1 lists the current characteristics of the W-band radar system that was used to measure the test target.

The in-phase and quadrature (I&Q) outputs of the system are digitized in the radar to 12-bit accuracy for each pulse. Four analog to digital (A/D) converters sample the vertical and horizontal I&Q returns from eight vertically transmitted pulses, followed by the returns from eight horizontally transmitted pulses for each of the 256 steps in frequency. Data collection is triggered when a preselected angle of rotation has been reached. The data are then demultiplexed, averaged over eight pulse groups, and stored as 256 I&Q pairs for both the vertical and horizontal receive channels. Time and turntable angle are also recorded with each ramp of data.

## 2.4 Measured Data

The target measurements were made on 9 June 1997, at the Aberdeen Test Center (ATC) outdoor high-resolution millimeter-wave (MMW) signature measurement facility at Airbase Range 8. The target was rotated  $370^\circ$ ; this range includes an extra  $5^\circ$  on either side of the  $0^\circ$  mark at the start and end of the rotation, which was to be used for checking signal level drift during the measurements. The raw data were calibrated with software developed by ARL [6]. The data consisted of I&Q values for 256 frequencies incrementally stepped between 93.488 and 95.0 GHz for four polarizations; these I&Q values were sampled every  $0.006^\circ$ . A ramp of data is defined as the I&Q values associated with all the linearly swept frequencies for a single polarization and aspect angle. The calibrated data were coherently

**Table 1. Radar characteristics at W-band.**

Parameter	Value
Maximum frequency	95.0 GHz
Minimum frequency	93.488 GHz
Rf bandwidth	1511.64 MHz
Frequency step	5.928 MHz
Peak transmitted power	+13 dBm
Pulse width	100 ns
Pulse repetition frequency	1.0 MHz
Transmitted polarization	V or H
Received polarization	V and H
3-dB beam width (two way)	4.4°
System noise figure	11 dB single sideband
Minimum detectable signal	-62 dBsm
Polarization isolation	30 dB

averaged over 1024 ramps, or approximately 6° segments, to form an I&Q offset. This offset was subtracted from each ramp of data in the segment.

To ensure that the 95-GHz radar was operating properly, I performed an error analysis on the calibration measurements, determining the amplitude and phase stability of a trihedral and a dihedral on a rotating mount. Figures 4 and 5 show the RCS and the variation in phase as a function of frequency for co-polarization for the dihedral rotated through 22.5°. I calculated the variation in phase by subtracting the phase associated with the frequency with index  $j$  from the phase of frequency with index  $j + 1$ , then properly unwrapping the phase difference. I then chose the 22.5° dihedral for analysis because it has a minimal impact on calibration. After each frequency was averaged over 2000 measurements, I found that the high frequencies have a lower signal to noise ratio (SNR). Further analysis indicated that only the last 20 frequencies were of poorer quality; these were eliminated from further analysis. Table 2 shows the standard deviation of the RCS and phase calculated over frequency with the last 20 frequencies eliminated. The small values indicate that the radar is functioning properly over the reduced bandwidth. Table 2 provides a lower bound for the measurement error.

## 2.5 Simulation Models

The radar returns were simulated with Xpatch, CADDSCAT, NcPDT, and a PSM. The simulations were run with version 2.1 of Xpatch (with frequency-domain analysis), beta version 1.6.6 of CADDSCAT, and version 1.2 of NcPDT with the program Nc128.f (Nc128.f required some small modifications). The geometric models input to the simulations were generated with ACAD (version 9.0c), a geometric modeling program developed by Lockheed Martin. I used the PSM to validate the processing software and to estimate the processing errors.

Each code has different capabilities. CADDSCAT and NcPDT simulations can be performed in both the near and far fields, while Xpatch simulations can be performed only in the far field. In NcPDT, simulations can be performed with a measured or simulated antenna pattern. Both CADDSCAT

Figure 4. RCS for a  $22.5^\circ$  dihedral averaged over 2000 measurements.

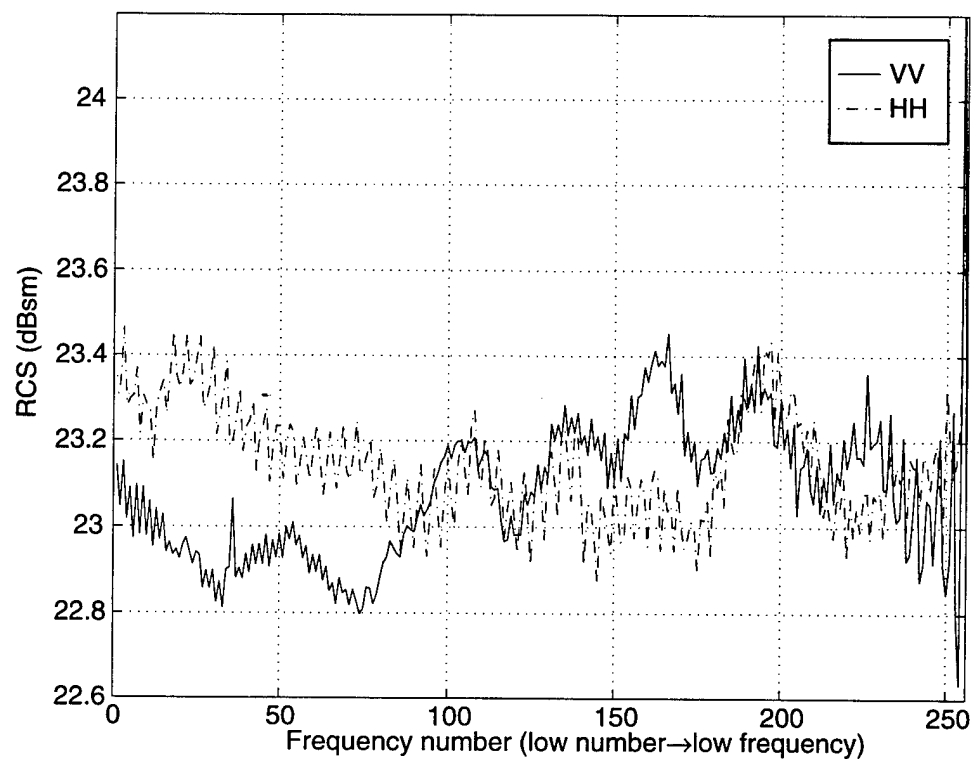
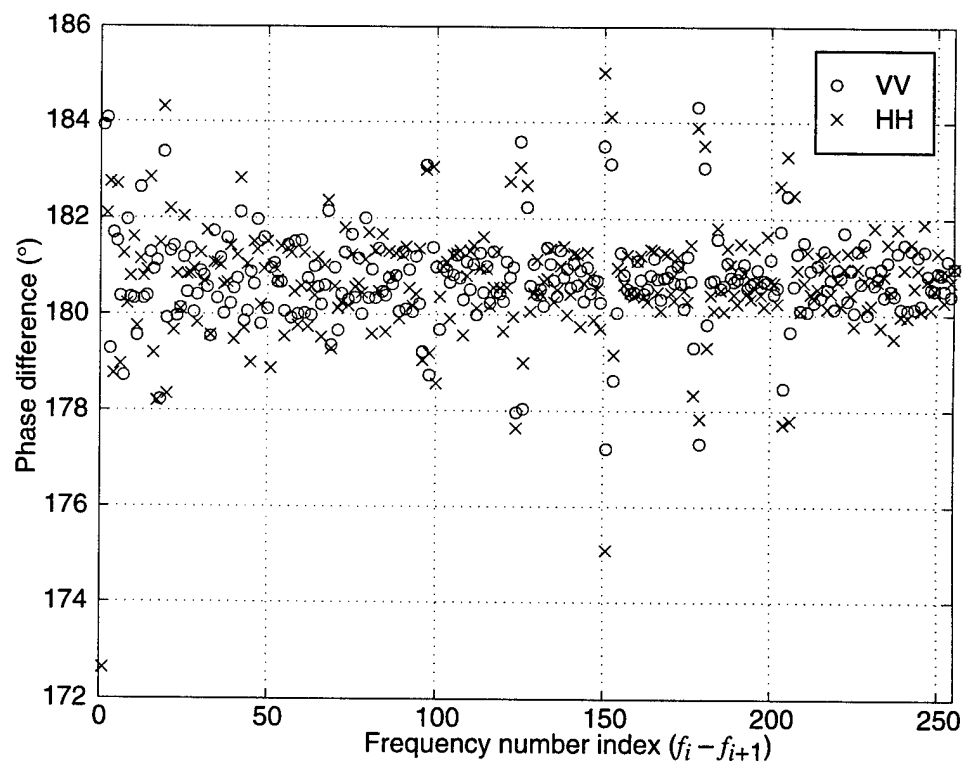


Figure 5. Phase variation for a  $22.5^\circ$  dihedral averaged over 2000 measurements.



**Table 2. Standard deviation of RCS and phase variation of 22.5° dihedral calculated over frequencies that have a high SNR.**

Polarization	RCS (dBsm)	Phase (°)
VV	0.15	0.8
HH	0.13	1.1

and Xpatch allow multiple-bounce simulations. None of the codes, however, can simulate traveling or creeping waves.

Far-field simulated data were generated with Xpatch, CADDSCAT, and a PSM that attempted to duplicate the measured data. The simulated aspect angles and frequencies matched the measurement parameters. However, the simulated antenna pattern was uniform, and the range was infinite. Because of symmetry, the simulations were run only from 0° to 90° in azimuth angle. I ran both predictive codes using a single-bounce calculation for a perfect electric conductor (PEC) with no edge diffraction or shadowing. The default integration densities were used. CADDSCAT was initially run with gap diffraction included, but the maximum contribution to the RCS was below -40 dBsm, so gap diffraction was subsequently omitted. Initially, a facet divergence file was included in the Xpatch simulation, but since it did not significantly affect the RCS, it was subsequently omitted.

Near-field simulated data were generated with CADDSCAT and NcPDT, and input into an RCS model that included a target/pylon interaction. The simulated range corresponded with the measurement range, but I reduced the number of frequencies and aspect angles to limit computation time. A single frequency was simulated for aspect angles near 90° azimuth angle. In CADDSCAT, I used a uniform antenna pattern, and in NcPDT, I used the measured antenna pattern. The PO calculations in NcPDT were performed with the first-order method and the default integration density, and the antenna pattern was assumed to be roll symmetric [3].

For CADDSCAT and NcPDT, the target model was represented in IGES 128 format, and for Xpatch in DEMACO facet model format. For CADDSCAT and NcPDT, each hemisphere and each complete cylinder contained 18 patches. For Xpatch, the target model contained 10,440 facets, and each hemisphere contained 4561 facets. The facet model was generated from the IGES 128 model by the conversion utilities bundled with Xpatch. The tolerance selected to generate the facets was 0.003 in., or 0.074 mm; this dimension is much smaller than the average wavelength used in the simulation (2.3 mm).

## 3. Procedure

### 3.1 Processing

I processed the radar data to reduce clutter and noise, correct for the effects of the antenna, and fine tune the RCS range correction. Figure 6 shows a block diagram of the processing procedure. Variables with capital letters represent signals in the frequency domain, and variables with small letters represent signals in the spatial domain. The input signal  $S$  was loaded, consisting of I&Q data for different frequencies and aspect angles. A Kaiser window ( $W$ ) then filters the signal to reduce blurring in the subsequent processed image. Next, a discrete Fourier transform (DFT) was performed to image the data, and then a bandpass ( $B$ ) filter was applied to remove clutter and noise outside the target region. An inverse DFT was performed to provide I&Q values, and an inverse of the original Kaiser window ( $W$ ) was applied. The transfer function is given by

$$H(z) = \frac{(SW) * b}{SW} , \quad (1)$$

where  $S$  is the I&Q data,  $W$  is the coefficients for the Kaiser window,  $b$  is the inverse DFT of the bandpass filter  $B$ , and the operator  $*$  denotes convolution.

The procedures used to process the data were *get*, *filter*, *image*, *extract*, *inverse*, and *bandwidth average*, as shown on the left side of the flow chart in figure 7. The procedures were implemented as functions in MATLAB (version 4.2). The major components of the procedures are shown on the right side of the figure. The components are divided between 1-D processing techniques (which I refer to collectively as the high-range resolution (HRR) processing technique) and 2-D processing techniques (which I refer to collectively as the inverse synthetic aperture radar (ISAR) processing technique). Several components shown in figure 7 are used by both techniques.

#### 3.1.1 Get Data

In the "get data" procedure, I&Q data were read from measured and simulated data files, or generated by a PSM. This step was simplified by the use of a common binary format for data storage. PSM data were generated separately.

#### 3.1.2 Filter

In the filter procedure, the data were filtered by a Kaiser window with  $\beta = 2$ , where the  $\beta$  parameter affects the sidelobe attenuation. If the HRR processing technique was selected, the Kaiser window was 1-D, and if the ISAR processing technique was selected, the Kaiser window was 2-D.

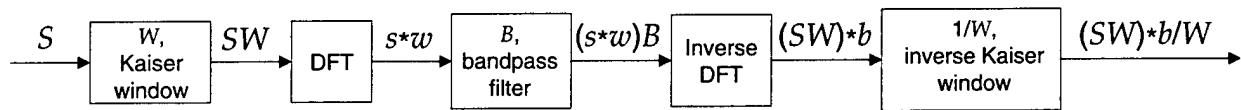


Figure 6. Signal flow diagram of data processing.

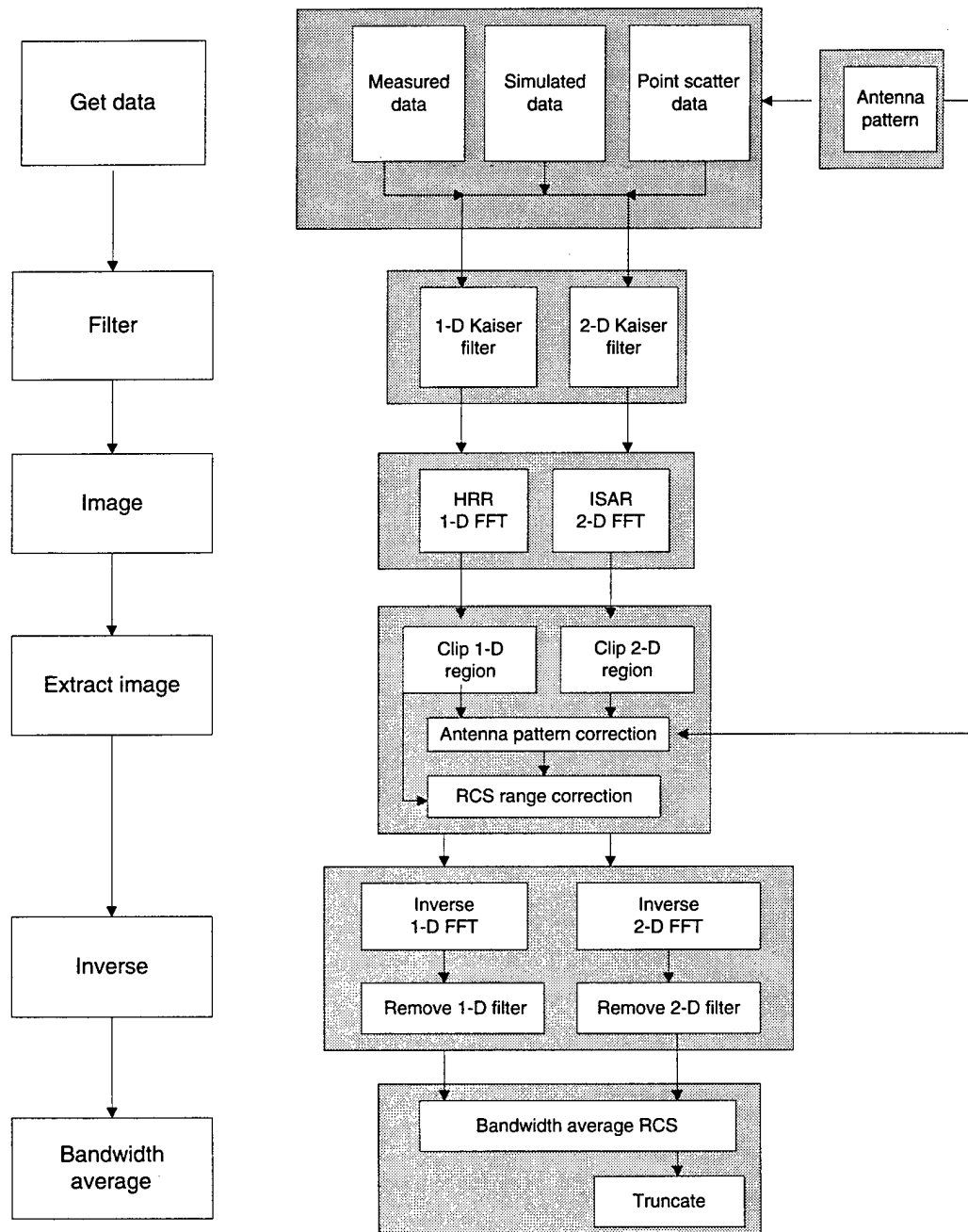


Figure 7. Flow chart for computing bandwidth-averaged RCS: (left) procedures and (right) major components.

### 3.1.3 *Image*

In the image procedure, a 1-D fast Fourier transform (FFT) was performed to generate an HRR profile, or a 2-D FFT was performed to generate an ISAR image.

### 3.1.4 *Extract*

In the extract procedure, the algorithm extracted the target from clutter and noise by clipping regions of the HRR profile or ISAR image. Initially, the extraction region was determined by target geometry and aspect angle. The image (or equivalently, the data) was divided into two regions, near broadside and head on, for which different extraction algorithms were employed. The near-broadside region was defined as within  $\pm 15^\circ$  of the broadside of the cylinder portion of the target, and the head-on region was defined as within  $\pm 75^\circ$  of the apex of either hemisphere. In the head-on region, the RCS was dominated by returns from the facing hemisphere, and in the near-broadside region, it was dominated by returns from the cylinder portion of the test target. In practice the division between the two regions is not smooth, so there will be a small discontinuity in the processed RCS.

The extraction algorithm used varied with the processing technique (ISAR or HRR) and image region. When the ISAR processing technique was applied in the head-on region, the extraction algorithm was based upon a diamond-shaped area that was translated and scaled. The center of the diamond corresponded to the location of the specular reflection from the appropriate hemisphere of the target. The size of the diamond was empirically determined, and it was scaled as a function of aspect angle. The shape of the diamond was not corrected for curvature, but the location of the center of the diamond with respect to the ISAR image was corrected.

For ISAR processing in the near-broadside region, the extraction algorithm was based upon a rectangle that was translated, rotated, scaled, and corrected for curvature. The rectangle corresponded to the geometry of the target, but was expanded and shifted downrange. An additional rectangular region was included for aspect angles that had a large specular return from the cylinder portion of the target. To encapsulate the sidelobes in the image, this area was added for aspect angles  $\pm 2.5^\circ$  from broadside. The center of the rectangle corresponded to the location of the specular return on the target.

For HRR processing in both regions, the extraction algorithm was based upon the target occupying a series of HRR cells. The center of the extraction region was calculated from the geometry of the target. The extraction procedure was modeled as a bandpass filter in the spatial domain, as shown in figure 7.

Figures 8 and 9 illustrate the different extraction regions for ISAR images at azimuth angles of  $0^\circ$  and  $88^\circ$  and an elevation angle of  $1.4^\circ$ , for VV po-

larization. The dotted lines in these figures denote the extraction region. The downrange and crossrange resolution is approximately 0.1 m. The contour line levels range from 10 to  $-40$  dBsm, in 10-dB intervals. The most prevalent contour level is  $-40$  dBsm.

Occasionally, significant blurring occurred in the image, which required the extraction region to be adjusted. The most likely cause was wind shaking the target, but meteorological data were not available to confirm this hypothesis. If the ISAR processing technique was used with the target

**Figure 8. ISAR image of target for region dominated by a hemisphere; diamond-shaped outline encloses target RCS.**

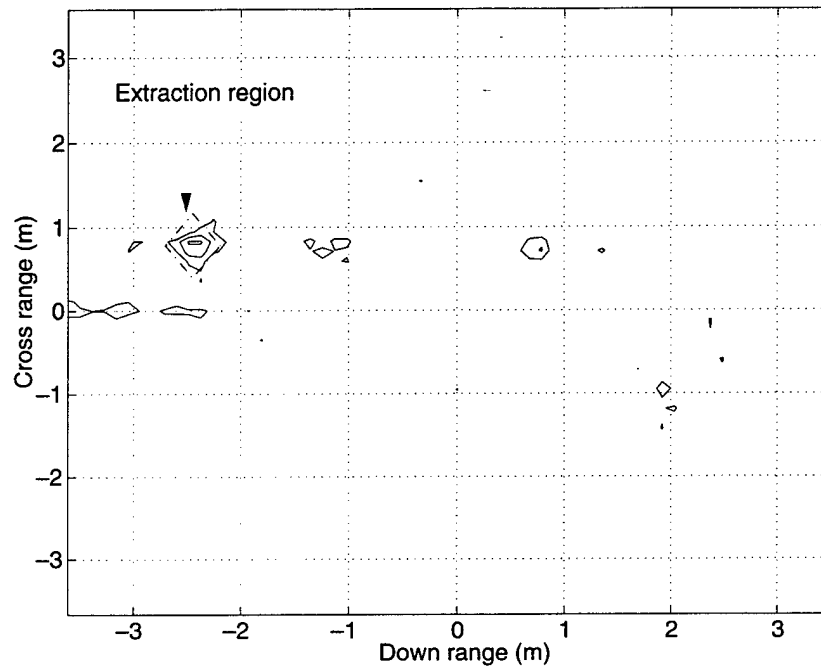
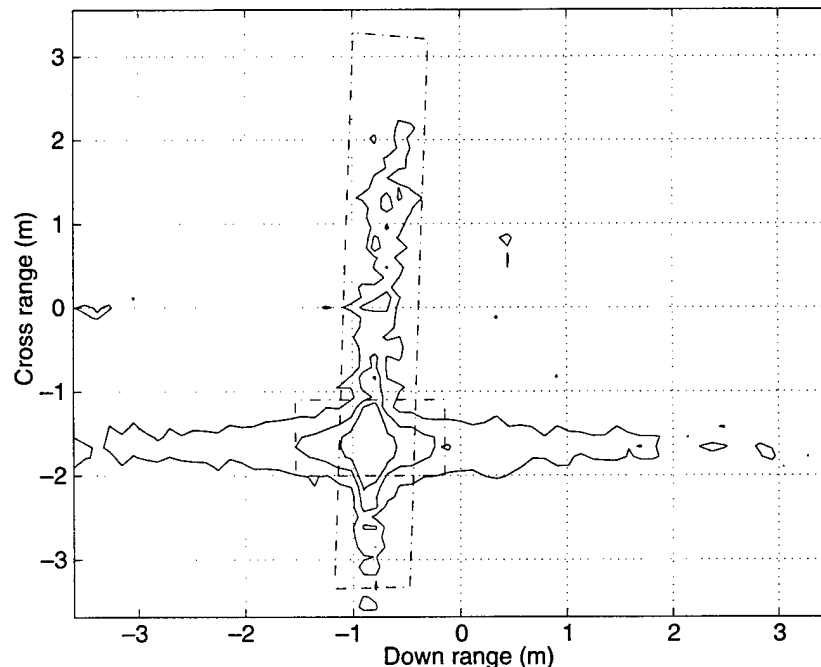


**Figure 9. ISAR image of target for region dominated by cylinder; trapezoid-shaped outline encloses target RCS.**





in the head-on region, and the computed standard deviation was greater than 2.4 dB, then the size of the extraction region was increased and the processing procedure was repeated. The size of extraction region was increased only once per ISAR image. I chose the threshold for the standard deviation by examining the processed data.

Next, if appropriate, I applied an antenna pattern correction to the data. The method used depended on the processing technique and region. If ISAR processing was used and the target was in the near-broadside region, then each cell in the image was divided by the antenna pattern value corresponding to its angular position. If the target was in the head-on region, all the extracted cells in the image were divided by a single antenna pattern value corresponding to the geometric location of the reflection point from the appropriate hemisphere.

For HRR processing, the same antenna pattern correction technique was used for the head-on region. But if the target was in the near-broadside region, the target was distributed in crossrange, so the effect of the antenna could not be removed in this way.

The last step in the extract procedure was a fine range correction of the RCS. Initially, the calibrated data were range corrected to the center of the target, 46.66 m. As the target aspect angle changed, the range to the specular reflection point on the hemispheres changed. This change was significant, since it could cause the RCS to change by as much as 0.8 dB.

### **3.1.5 *Inverse***

In the inverse procedure, the modified image was converted back to I&Q values by a 1-D or 2-D inverse FFT algorithm. I removed the Kaiser window by multiplying the I&Q values by the inverse of the filter coefficients, then normalizing the RCS so that power was conserved.

### **3.1.6 *Bandwidth Average***

In the bandwidth-averaging procedure, the I&Q values were converted to RCS, then averaged over frequency. If the ISAR technique was used to process the data, bandwidth-averaged RCS values were truncated at the beginning and ending aspect angles of the ramps of data that were used to generate an image. This step was necessary to minimize the effect of the convolution performed in equation (1). I calculated the number of values truncated by taking the number of ramps used to generate the ISAR image, then dividing by 8. For example, if 32 ramps were used to generate the ISAR image, then the first and last four RCS values were eliminated. The RCS values at the remaining aspect angles were normalized so that the same average RCS was maintained.

### 3.2 Antenna Pattern

A 1-D measured antenna pattern was calculated from a raster scan of a reflector at a range of 47 m. First the data were filtered along the  $0^\circ$  elevation scan by a 2-D finite-duration impulse response (FIR) smoother. Then, the data were clipped and fit to a second-degree polynomial. The filtered antenna pattern was normalized by its maximum value, and its angle look-up table was offset to the peak location of the fitted polynomial. Figure 10 shows the resulting two-way, 1-D antenna pattern for VV polarization. The two-way beam width is approximately  $4.4^\circ$ . This is smaller than the angular extent of the cylinder portion of the target at broadside, which is  $5.7^\circ$ . The peak of the antenna pattern was offset from  $0^\circ$  azimuth angle by  $0.66^\circ$ .

### 3.3 Parameters

I evaluated the effects of varying several parameters used in the HRR and ISAR processing techniques, performing the analysis over a subsection of the head-on region to increase accuracy. (I determined the region by examining the processed RCS results.) Figure 11 shows a graph of the unprocessed and processed bandwidth-averaged RCS obtained by the 128-ramp ISAR processing technique. The plot of the unprocessed RCS indicates that the noise/clutter in the head-on region is approximately  $-3$  dBsm, which is significantly higher than the predicted RCS of approximately  $-15$  dBsm. The low-noise, head-on region was determined to be between azimuth angles of  $0^\circ$  to  $60^\circ$ ,  $120^\circ$  to  $240^\circ$ , and  $300^\circ$  to  $360^\circ$ , as illustrated by the vertical lines in figure 11. For aspect angles near the transition between the head-on and the near-broadside region, an increase in the RCS was observed. The discontinuity between the two regions was caused by an increase in the noise (due to the use of a larger target extraction region) and by an increase in the RCS of the target.

Figure 10. Two-way azimuth angle antenna pattern for VV polarization.

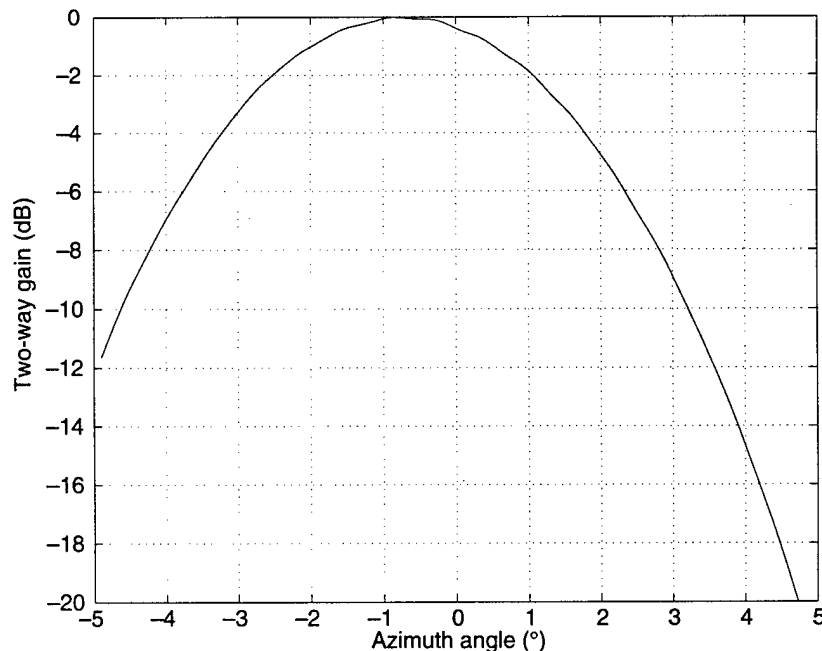
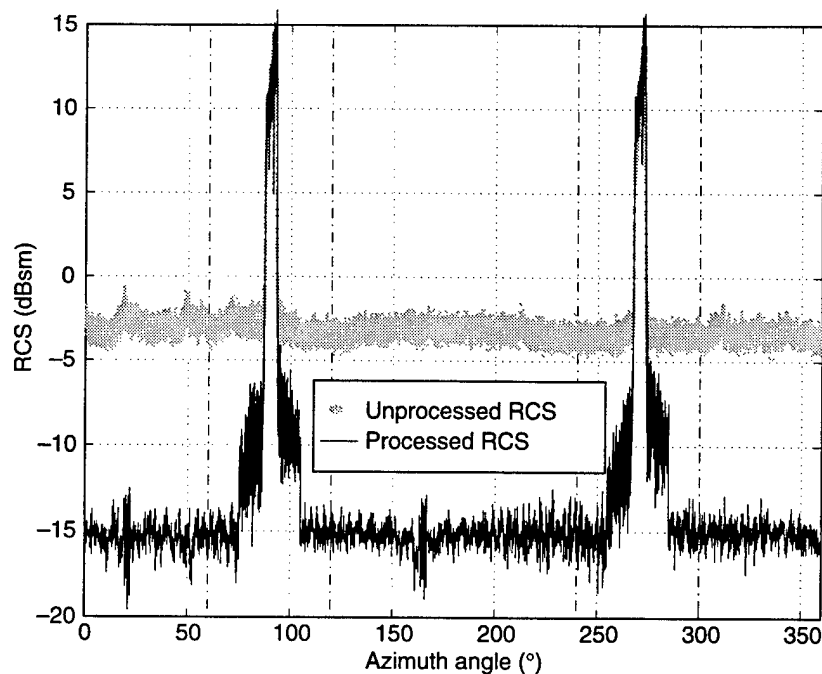


Figure 11. Bandwidth-averaged RCS unprocessed and processed with 128-ramp ISAR technique. Vertical lines show RCS low-noise, head-on region; unprocessed RCS curve is higher.



To evaluate the processing techniques, I calculated for each technique the average and the standard deviation of the bandwidth-averaged RCS in the low-noise, head-on region. The results were then smoothed by a 144-point moving-average filter. This filter was selected because the 192-ramp ISAR image resulted in 144 RCS values after clipping. Therefore, the filter data results should show the trade-offs between the coherent integration gain achieved in ISAR imagery and the noncoherent integration achieved through smoothing. The 192-ramp ISAR image should have less noise because it has coherent integration and a smaller extraction region, but it is more susceptible to variations in the measurement system over time. If more ramps of data were used, the image would require additional processing to compensate for range migration and polar format data. The results are shown in table 3.

I calculated the RCS means by averaging (in meters squared) over aspect angle, then converting to units of decibel-square meter. The RCS standard deviations were calculated in meters squared, then added and subtracted to the mean value. The two sums were converted to decibel-square meter, and then their difference was calculated and divided by two. As long as the mean is much larger than the standard deviation, the upper and lower bounds calculated from the standard deviation are symmetric (which was the case). This technique was used in calculating the standard deviation in the subsequent tables.

The results from table 3 indicate that the ISAR processing technique was better than the HRR processing technique and that the number of ramps used to generate an ISAR image did not make a significant difference in the mean or the filtered standard deviation. The standard deviation was slightly reduced as the number of ramps in the ISAR image was increased.

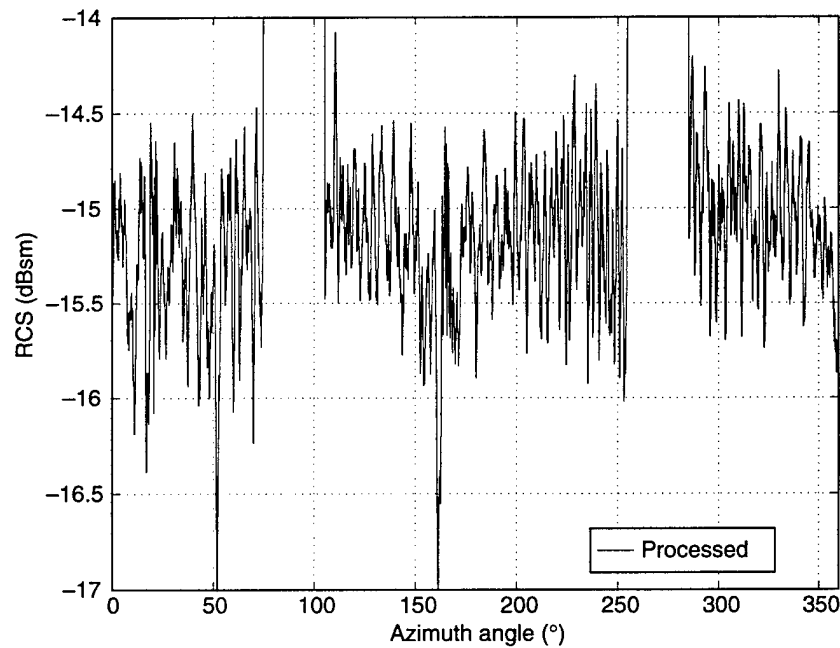
The RCS results processed with 128-ramp ISAR images were selected for further analysis. Figure 12 shows the RCS processed with the 128-ramp ISAR technique. The data are usually stable, with brief segments of high variability (probably caused by the wind shaking the target).

For the near-broadside region, both the HRR and the 32-ramp ISAR processing techniques were used in calculating the measured RCS. An antenna pattern correction was applied only to the ISAR image. The RCS was not averaged over aspect angle, since the SNR was much higher and there were significant variations in RCS.

**Table 3. Standard deviation calculated for low-noise region dominated by returns from hemispheres.**

Processing technique	Mean $\pm$ SD (dBsm $\pm$ dB)	Smoothed SD (dB)
ISAR 32	$-14.79 \pm 0.82$	0.37
ISAR 64	$-14.85 \pm 0.67$	0.36
ISAR 128	$-14.93 \pm 0.63$	0.36
ISAR 192	$-14.89 \pm 0.58$	0.34
HRR 1	$-14.17 \pm 1.85$	0.73
HRR 2	$-13.45 \pm 1.83$	0.94

**Figure 12. Bandwidth-averaged RCS smoothed with a 144-point moving-average filter.**



## 4. Results

The measured RCS data were processed and the results compared with simulated and theoretical RCS predictions. I analyzed the agreement for two regions of the target, but not for a third, transitional region. As previously discussed, I initially divided the target into the broadside and the head-on regions. However, near the transitions between these two regions, both the simulated and measured data had limitations. Although the RCS of the measured data had not increased significantly, I had to increase the size of the extraction region significantly to account for nonspecular scattering. This size increase lowered the SNR. Further, the simulations could not model secondary scattering effects. Because of these limitations, I made no comparisons between measured and simulated data in this transition region.

I did analyze a limited broadside region and a limited head-on region. The broadside region was clearly defined by the RCS reduction and was limited to approximately  $\pm 3^\circ$  from broadside of the cylinder. To avoid noise and processing problems, I limited the head-on region to  $\pm 60^\circ$  from the apex of either hemisphere; I refer to this region as the low-noise, head-on region.

### 4.1 Theory and Near-Field Model

I performed a theoretical calculation of the RCS using high-frequency, perfect electrically conducting, monostatic approximations. The RCS ( $\sigma$ ) of a sphere in the far field is given by

$$s = \pi a^2 \text{ for } ka > 20, \quad (2)$$

where  $a$  is the radius of the sphere and  $k$  is the propagation number. For a 4-in. sphere at 94.149 GHz (the average usable radar frequency),  $\sigma = -14.89$  dBsm and  $ka \approx 200$ . Applying the standard far-field criterion, range  $> 2D^2/\lambda$ , results in a range of 26 m. Since this is smaller than the measurement range of 46.6 m, the far-field approximations should be valid.

At broadside, no theoretical RCS could be calculated and compared to measured RCS because of several complicating factors. The cylinder portion of the target is approximately 4.6 m long (so that this portion is in the near field), the antenna pattern is not uniform, and the pylons supporting the target had a significant effect on the RCS. However, I was able to develop a near-field model that incorporated these elements.

The near-field model for the RCS is based upon the linear superposition of electric fields induced by the portion of the target that was covered by the pylons and those induced by the portion not covered by the pylons. The model for the pylons did not attenuate the electric field, but it did produce a phase shift in the electric field. The modeled RCS was calculated from

$$\sigma = \left| E_t(i,q) + E_p(i,q) e^{j\varphi} \right|^2, \quad (3)$$

where  $\sigma = \text{RCS}$ ,  $E_t$  is the electric field of the target not covered by the pylon,  $E_p$  is the electric field of the target covered by the pylon, and  $\phi$  is the phase shift associated with the pylon. For CADDSCAT, I applied equation (3) directly. For NcPDT, I simulated the phase shift associated with the pylons by changing the range to the pylons. For the model results obtained with CADDSCAT simulated data, I had to apply an antenna pattern correction to the measured data. On the other hand, the model results obtained with NcPDT simulated data could be compared directly with the measured data.

The RCS was simulated as a function of phase shift. I selected an appropriate phase shift by matching gross features of the measured and modeled RCS. I theoretically estimated the phase shift using

$$\phi = 4\pi \frac{(\sqrt{\epsilon} - 1)d}{\lambda}, \quad (4)$$

where  $\epsilon$  is the dielectric constant of buoyant Styrofoam,  $d$  is the thickness of the Styrofoam, and  $\lambda$  is the transmitted wavelength. According to Knott et al [7], a typical value for the dielectric constant of Styrofoam is 1.04. For  $\epsilon = 1.04$ ,  $d = 1/4$  in., and  $\lambda = 3.2$  mm, the phase shift is  $28^\circ$ . (The pylons also have a noncoherent return, but it was much smaller than the RCS of the target, so it was not included in the model.)

## 4.2 Comparison of Simulation, Theory, and Measurement

### 4.2.1 Hemispheres

I simulated the RCS for aspect angles dominated by returns from the hemispheres using CADDSCAT and Xpatch, and compared the results to theoretical and measured values. The results are presented in two categories: unsmoothed and smoothed. Within these two categories are both processed measured data and simulated data. The measured data consisted of RCS bandwidth-averaged statistics that were obtained with the ISAR processing technique on 128 ramps of data. Simulated data consisted of RCS bandwidth-averaged data obtained with Xpatch and CADDSCAT. (The simulated data did not have to be processed for clutter and noise reduction.) *Smoothed data* were smoothed with an 83-point or  $0.5^\circ$  azimuth angle moving-average algorithm.

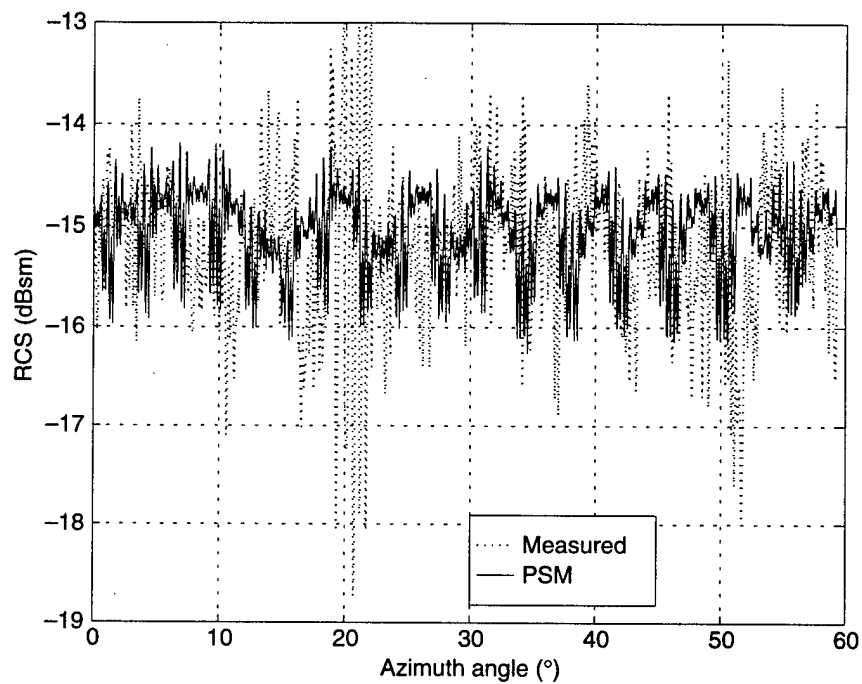
Analysis of the data indicated that the RCS statistics that were dominated by returns from the hemispheres should be compared (for the simulated data) for azimuth angles between  $0^\circ$  and  $60^\circ$ , and (for the measured data) for the low-noise head-on region (four  $60^\circ$  regions). The SNRs for the measured data were higher at these aspect angles because the antenna beam fully illuminated the target. Also, the location of specular return did not move significantly during the formation of an ISAR image with respect to a range cell.

Table 4 shows the mean and standard deviation of the bandwidth-averaged RCS. Figures 13 and 14 show a plot of the processed RCS values.

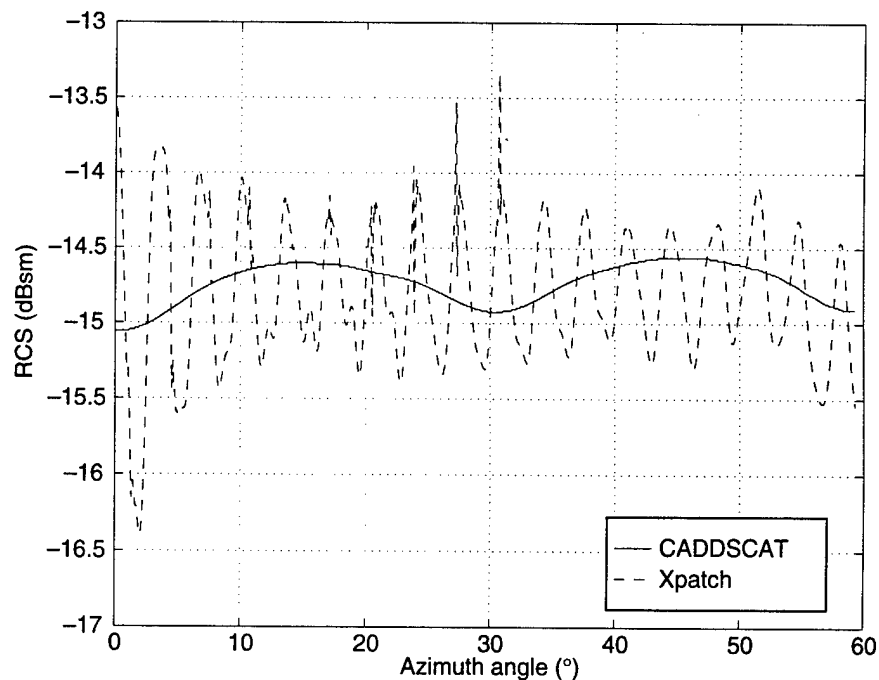
**Table 4. Measured and simulated RCS values for returns dominated by a hemisphere.**

Processing	Measured (dBsm $\pm$ dB)	Xpatch (dBsm $\pm$ dB)	CADDSCAT (dBsm $\pm$ dB)	PSM (dBsm $\pm$ dB)	Theoretical (dBsm $\pm$ dB)
Unsmoothed	$-14.93 \pm 0.63$	$-14.93 \pm 0.48$	$-14.90 \pm 0.14$	$-14.94 \pm 0.38$	$-14.89 \pm 0$
Smoothed	$-14.93 \pm 0.36$	$-14.93 \pm 0.45$	$-14.90 \pm 0.13$	$-14.94 \pm 0.25$	$-14.89 \pm 0$

**Figure 13. Bandwidth-averaged RCS values for measured data and a point scatter model.**



**Figure 14. Bandwidth-averaged RCS values for Xpatch and CADDSCAT simulation.**



The amount of data in the plots has been reduced by a factor of 10 to improve readability.

The results from table 4 indicate that the average RCS of each data set agreed with the theoretical predicted RCS to within the corresponding standard deviation. The simulation run using CADDSCAT was able to predict the RCS more accurately and precisely than the simulation run using Xpatch, but significantly more computer processing time was required. The PSM average RCS was approximately equal to the average measured RCS, which indicates that the processing had a minimal effect on the signal. The standard deviation of the PSM represents the processing noise. There is a trade-off between the amount of processing noise and the reduction in measurement system noise. Assuming independent white noise, the signal to processing noise ratio for the measured RCS is 2.4 dB:

$$\text{SNR} = 10 \log_{10} \frac{P_s}{P_n} = 10 \log_{10} \frac{0.63^2 - 0.38^2}{0.38^2} = 2.4 \text{ dB} , \quad (5)$$

where  $P_s$  is signal power and  $P_n$  is processing noise power.

#### 4.2.2 Cylinder

I simulated the RCS of returns dominated by the cylindrical portion of the target using CADDSCAT and NcPDT for aspect angles near 90° and compared the results to measured data. The measured data were processed with and without an antenna pattern correction included in the calculations, as described in section 3.1.4. The CADDSCAT simulation required a uniform antenna pattern and NcPDT used the measured antenna pattern. Correcting for the antenna pattern slightly degraded the data, but the major peaks and troughs of the data remain. I calculated the near-field RCS in NcPDT using the definition introduced by Wang [8]:

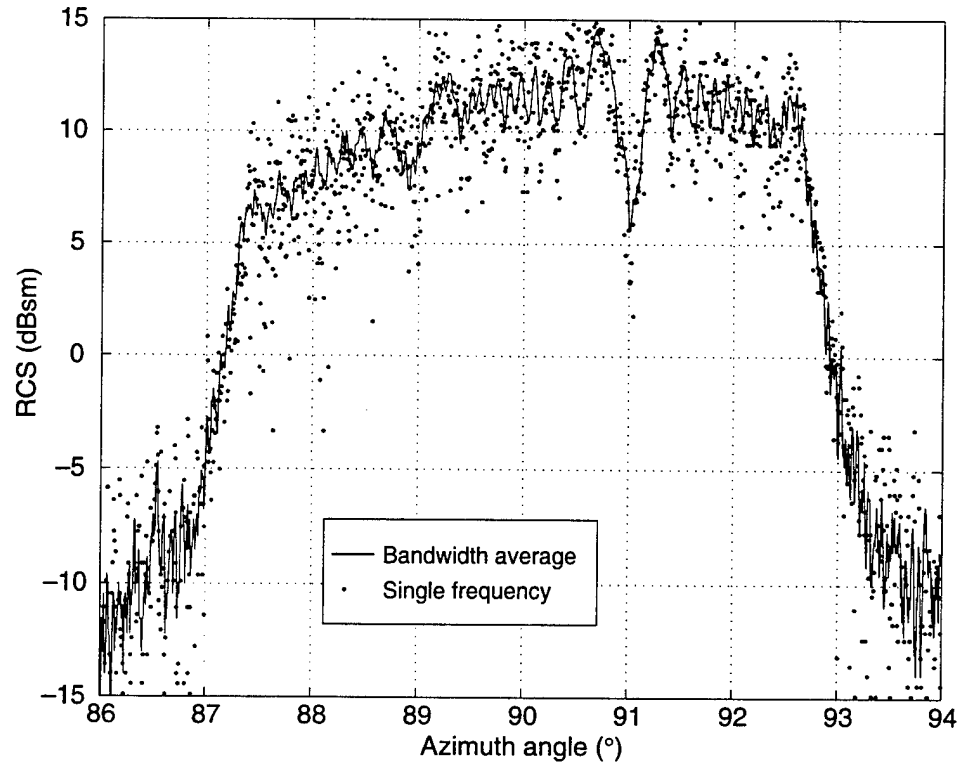
$$\frac{P_2}{P_1} = \frac{\sigma_1}{4\pi} \left[ \frac{\lambda G_{\max}}{4\pi R^2} \right]^2 , \quad (6)$$

where  $P_1$  is power transmitted,  $P_2$  is power received,  $\sigma_1$  is the near-field RCS,  $G_{\max}$  is the maximum antenna gain, and  $R$  is the range to the center of the target. This is equivalent to how the measured RCS values were calculated.

Initially, I processed the measured data to determine the variation in RCS over frequency for all broadside aspect angles except those that were highly attenuated. These returns were believed to be significantly affected by the supporting pylons, and the RCS of these returns for different frequencies fluctuated. I determined the region for analysis by examining the relative peaks in the RCS of the measured data. Figure 15 shows the bandwidth-averaged RCS and the RCS of a single frequency versus aspect angle. The vertical lines show the aspect angles that were initially analyzed. The standard deviation of the bandwidth-averaged RCS was 7.3 dBsm and the variation over frequency was 5.2 dBsm. I calculated the



Figure 15.  
Bandwidth-averaged  
and single-frequency  
RCS for measured  
data.



latter by taking the square root of the average of the RCS variance over frequency for each aspect angle. The result indicates that there is more variation over aspect angle than over frequency, suggesting that bandwidth averaging is reasonable. Another indication that bandwidth averaging will be necessary is that the RCS model was not detailed enough to exactly reproduce the constructive and destructive interference for each frequency at each aspect angle.

To calculate the RCS for the average usable radar frequency of 94.149 GHz, I began by using NcPDT and CADDSCAT to calculate the electric fields for two sections of the test target: the section not obscured by the pylons and the sections obscured by the pylons. The RCS was then calculated by application of equation (3). A phase delay was first inserted into the electric field calculated for the section obscured by the pylons, and the result was then superimposed on the electric field calculated for the other section. Figures 16 and 17 show the effects of different phase delay on the RCS simulated with NcPDT and CADDSCAT. The NcPDT simulation included the measured antenna pattern in the calculations.

I selected a reasonable phase delay by comparing the results from figure 15 with the results from figure 16 and 17: I found the measured reductions in the RCS at aspect angles that roughly corresponded to the locations of the pylons and matched these reduced RCS values to simulated results. A phase delay of  $\pi/2$  or  $90^\circ$  was selected for more detailed analysis. This is considerably larger than the predicted phase shift of  $28^\circ$ , which was too

Figure 16. RCS calculated with CADDSCAT for different phase delays.

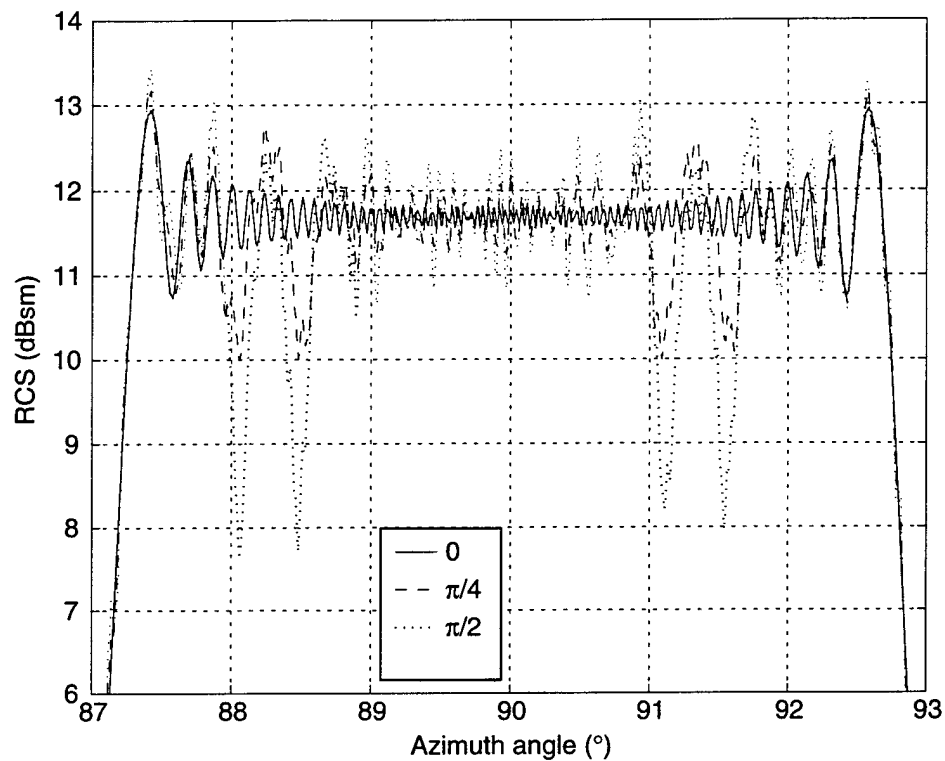
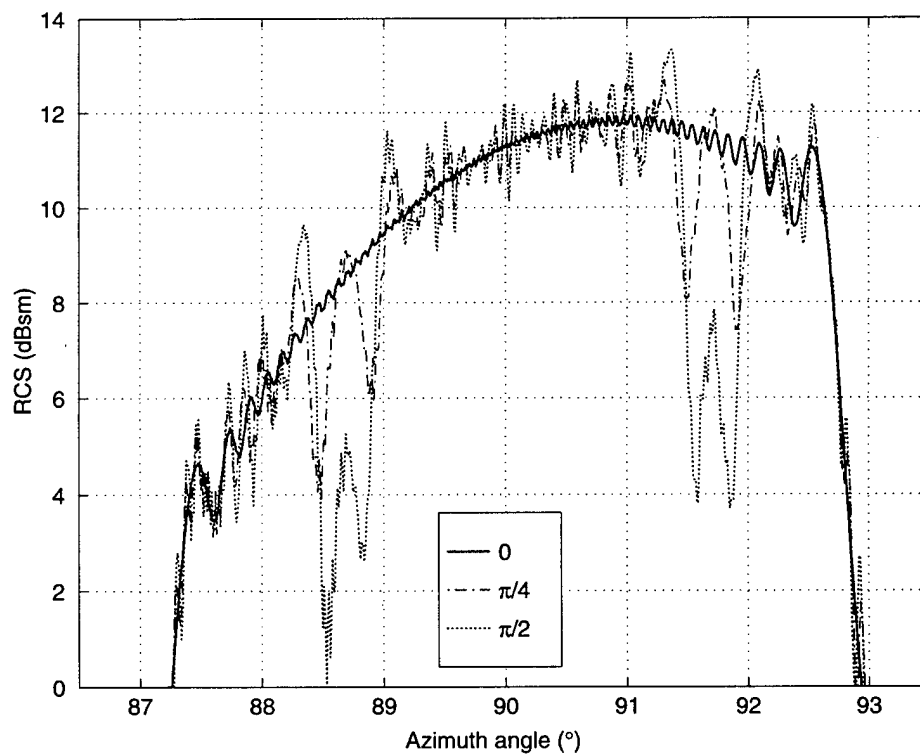


Figure 17. RCS calculated with NcPDT for different phase delays.



small to produce the variations found in the measured data. (I could have selected a smaller phase delay for analysis, but the larger phase shift accentuated the phenomenon of interest.)

Figures 18 and 19 show the measured bandwidth-averaged RCS and the simulated RCS for the middle frequency with a phase delay of  $90^\circ$ . In figure 18, an antenna pattern correction was applied to the measured data, and then a linear adjustment was performed. (This linear adjustment was required because the original antenna pattern correction was not sufficient. Rather than readjust the antenna pattern and the data, I performed a linear correction as a function of aspect angle.) The adjusted data were used for

**Figure 18.** RCS calculated with CADDSCAT and measured RCS processed with antenna pattern corrections.

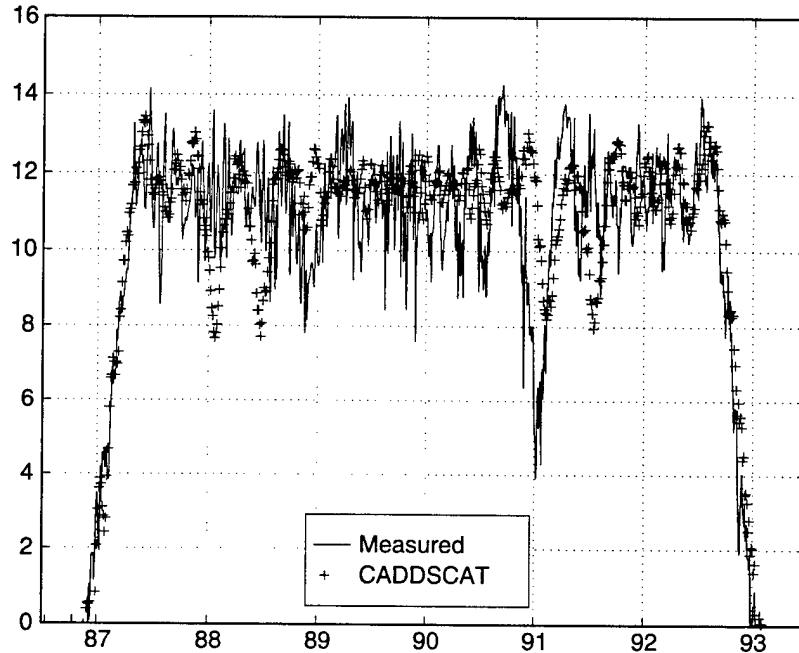
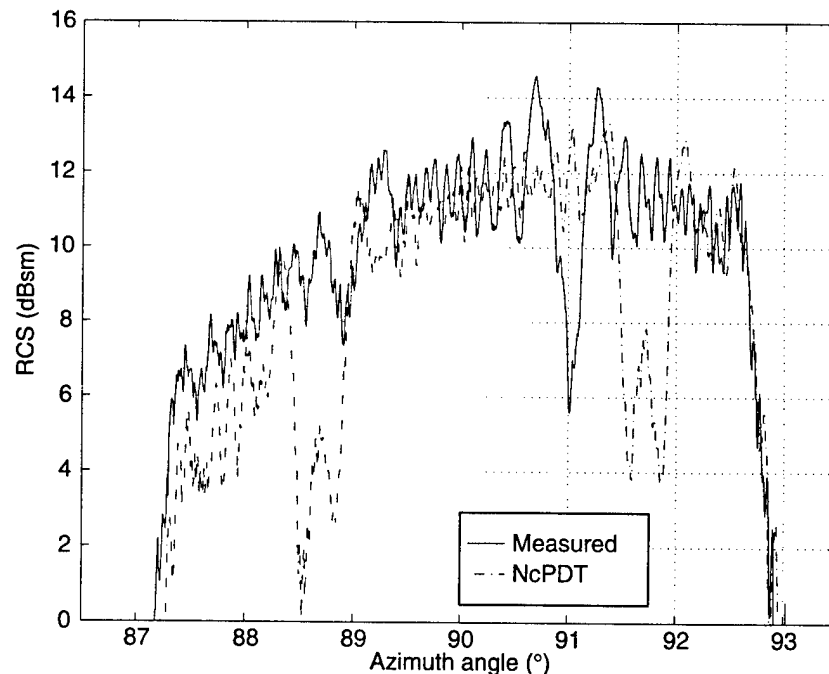


**Figure 19.** RCS calculated with NcPDT and measured RCS processed without antenna pattern corrections.



further analysis. The results from NcPDT are also slightly off from measured results, but the difference is less. No correction was applied to these data.

Figures 18 and 19 show that the shape and the location of the nulls in the simulated data do not correspond with those in the measured data. The lack of agreement on the location of nulls indicates that the actual interaction with the pylons is more complex than the modeled interaction. The pylons are curved 3-D objects with normals that are different from those of the target. Because of this curvature, both the direction and phase of electromagnetic radiation propagating through the pylons could change relative to free space. These changes could account for a change in position of the RCS nulls and their shape.

A point-for-point comparison is not appropriate for the data in figures 18 and 19 because of the difference in the nulls in the measured and simulated results, the aspect angle sensitivity of the data, and the expected limitations in the target model. However, other meaningful quantities can be analyzed. Tables 5 and 6 quantitatively describe the agreement between measured and simulated RCS for aspect angles near broadside.

Table 5 shows the crossover angles at which the major contributor to the RCS changed from the cylinder to the hemisphere, as well as the mean and standard deviation of the RCS between those angles. The crossover angles were defined as the angles at which simulated and measured RCS exceeded a threshold. The thresholds were chosen based upon the RCS of the target at broadside and effects of the antenna pattern. For the measured data, the thresholds were 4 and 7 dBsm with respect to crossover angles 1 and 2. For NcPDT, the thresholds were 3 and 7 dBsm. For the measured data with an antenna pattern correction and CADDSCAT, both thresholds were 9 dBsm.

The measured and simulated results shown in table 5 are in agreement. The simulated and measured mean RCS and standard deviations are ap-

**Table 5. Crossover angles and RCS statistics.**

Data type	Crossover angle 1 (°)	Crossover angle 2 (°)	RCS mean $\pm$ SD (dBsm $\pm$ dB)
Measured	2.65	2.69	10.7 $\pm$ 2.0
NcPDT	2.64	2.74	9.7 $\pm$ 2.6
Measured (antenna pattern corrected)	2.70	2.76	11.5 $\pm$ 1.3
CADDSCAT	2.78	2.72	11.5 $\pm$ 0.9

**Table 6. Mean and standard deviation of RCS and energy density spectrum statistics for data with nulls removed.**

Data type	RCS mean $\pm$ StD (dBsm $\pm$ dB)	Frequency mean $\pm$ SD (1/° $\pm$ 1/°)
Measured	10.7 $\pm$ 2.2	5.6 $\pm$ 1.3
NcPDT	9.8 $\pm$ 1.5	3.6 $\pm$ 0.9
Measured (no antenna pattern correction)	11.7 $\pm$ 2.0	5.7 $\pm$ 1.7
CADDSCAT	11.9 $\pm$ 1.1	4.0 $\pm$ 0.9

proximately equal, as are the crossover angles. The results for the data with the measured antenna pattern are slightly narrower than those for data without an antenna pattern; this difference is to be expected, since a narrow antenna pattern would attenuate the RCS near the crossover angles. The mean RCS results from NcPDT are slightly lower and are probably the result of several small errors. The antenna pattern was assumed to be stationary during the simulation, but because the target was offset from the center of the turntable, the antenna pattern moved with respect to the target. This move had a small effect on the range and aspect angle. To account for this effect, I adjusted the measured crossover angles in table 5 by  $0.045^\circ$ .

Table 6 shows the results of a qualitative analysis of the RCS and energy density spectrum statistics for angles near broadside with the nulls removed from both the measured and simulated data. The starting and ending points for the data were determined by a threshold value that was 2 dB higher than the values used to determine the crossover frequencies in table 5. The data associated with a null were characterized as starting from a peak RCS, proceeding to a minimum RCS, and ending at a peak RCS. The mean and standard deviation of RCS and the energy density spectrum statistics were calculated for these data. The energy density spectrum statistics characterized the mean and standard deviation of the spectrum of the RCS, given by

$$\langle w \rangle = \sum w |S(w)|^2 \Delta w , \quad (7)$$

$$B = \left[ \sum (w - \langle w \rangle)^2 |S(w)|^2 \Delta w \right]^{1/2} , \quad (8)$$

where  $|S(w)|^2$  is equal to the energy density spectrum. I computed the spectrum by estimating the autocorrelation function using a triangle or Bartlett window, then performing a padded FFT [9]. A noise threshold was established in the energy density spectrum, and values below the threshold were set to zero. Also, the dc component in the energy density spectrum was set to zero. The results are shown in table 6.

The results in table 6 indicate that although the model could not reproduce the variations in the RCS seen in the measured data, the gross features were simulated. The standard deviation of the RCS for the measured data was higher than that of the modeled data. Also, the mean and standard deviation of the energy density spectrum of the measured data were higher than for the simulated data. The differences were not great, indicating that the modeled results roughly corresponded to those of the measurements.

## 5. Conclusion

The RCS of a test target that consisted of a cylinder with hemispherical ends was measured and modeled, and the results were evaluated. The target was measured with ARL's W-band, frequency-agile, instrumentation radar at ATC. The target was placed on a turntable, and radar measurements were made from  $-5^\circ$  to  $365^\circ$  azimuth angle. The data were calibrated, and then a methodology was developed to reduce clutter and noise. The radar return of the test target was simulated with CADDSCAT, Xpatch, NcPDT, and a PSM. These codes cannot predict scattering due to traveling or creeping waves, but for most aspect angles these phenomena appear negligible. Since such secondary scattering was not significant, I could eliminate noise and clutter by processing the measured data with narrow target-extraction regions that focused on the specular return of the target. The methods used to process and simulate the target returns depended on the aspect angle. The target was divided into two regions: head on and broadside. The RCS of the target in the head-on region was dominated by radar returns from the hemispheres, and that of the near-broadside region was dominated by returns from the cylinder. Subsections of these regions were further evaluated.

The bandwidth-averaged RCS statistics of the low-noise section of the head-on region were evaluated. Measured and simulated results were all in close agreement with the theoretical predicted RCS. The CADDSCAT simulation was more precise than the Xpatch simulation, but it was also more computationally intensive. The measured results demonstrated that these simulations could accurately extract RCS data from radar signals with a low SNR. Specifically, hemispheres with a theoretical RCS of  $-14.9$  dBsm were measured in noise and clutter that had an average RCS of  $-3$  dBsm. After the measured data were processed, the bandwidth-averaged RCS was  $-14.9$  dBsm  $\pm 0.6$  dB.

Analysis of the broadside region indicated that there was an interaction between the test target and supporting pylons. The test setup was configured to minimize the clutter and noise in the head-on region; as a side effect, this configuration increased the clutter in the near-broadside region. The target/pylon interaction was simulated by an RCS model, for which input was generated by NcPDT and CADDSCAT. Although the model could reproduce some of the statistics of the measured data, there were significant discrepancies. Simulated and measured results were in agreement for the measured crossover angles of high-to-low RCS and average RCS. On the other hand, the nulls and spectral characteristics of the RCS between the crossover angles were not in close agreement, although they had similar gross features. Because the interaction between the target and the pylons had not been anticipated, careful measurements were not taken that would allow detailed modeling of this phenomenon. Better measurements of the setup might have improved the model results. Future measurements should strive for a pylon configuration that does not lead to excessive interference at any given aspect angle, since one never knows for what purpose the data will be used.

## Acknowledgments

I would like to acknowledge and thank my colleagues for their contributions. Suzanne Stratton helped to collect, download, and unpack measured data, and to write the sections describing the radar and the target. Bob Bender, Bob Tan, and Don Testerman helped collect the data. Bruce Wallace contributed in the development of the radar system and the analysis of the data. Herb Dropkin contributed to the development of RCS model, and Jerry Silvius contributed to the development of the ISAR processing software. Peter Cremona-Simmons and Tom Pizzillo helped with ACAD modeling, and John McCorkle, Barry Scheiner, and Roberto Innocenti provided insights on signal processing. Jim Roedder of Boeing/McDonnell Douglas provided support for the modeling code CADDSCAT.

## References

1. M. Richard and J. Watson, *Data Analysis and Modeling: Near-Field Signature Model Study Final Report*, Nichols Research Corporation for Wright Laboratory/Armament Directorate, CDRL A004.
2. S. W. Lee, *Xpatch: A High Frequency RCS Computation Code for Facet Targets and Curved Patches*, DEMACO Technical Report (August 1992).
3. D. M. Elking, J. M. Roedder, D. D. Car, and S. D. Alspach, *A Review of High-Frequency Radar Cross Section Analysis Capabilities at McDonnell Douglas Aerospace*, IEEE Antennas Propag. Magazine **37**, No. 5 (October 1995), 33-43.
4. S. W. Lee and S. K. Jeng, *NcPDT-1.2: A High Frequency Near-Field RCS Computation Code Based on Physical Theory of Diffraction*, DEMACO, Final Report for Subcontract DI-SC-90-012 (June 1991).
5. H. Ling, R. C. Chou, and S. W. Lee, *Shooting and Bouncing Rays: Calculating the RCS of an Arbitrarily Shaped Cavity*, IEEE Trans. Antennas Propag. **37** (1989), 194-205.
6. R. L. Bender, *Use of a Remotely Controlled Dihedral for Calibrating a Polarimetric Radar*, Army Research Laboratory, ARL-MR-318 (June 1996).
7. E. F. Knott and T.B.A. Senior, *Studies of Scattering by Cellular Plastic Materials*, University of Michigan, Radiation Laboratory, Report No. 5849-1-F (April 1964).
8. H.T.G. Wang, *Near-Field Fuzing Simulation Studies, Part 1: Cylinder and Plate Targets (U)*, Naval Weapons Center (February 1987). (DTIC AD-C040 956) (SECRET)
9. A. V. Oppenheimer and R. W. Schafer, *Digital Signal Processing*, Prentice-Hall, Inc. (1975), pp 539-543.



## Distribution

Admnstr  
Defns Techl Info Ctr  
Attn DTIC-OCP  
8725 John J Kingman Rd Ste 0944  
FT Belvoir VA 22060-6218

Ofc of the Dir Rsrch and Engrg  
Attn R Menz  
Pentagon Rm 3E1089  
Washington DC 20301-3080

Ofc of the Secy of Defns  
Attn ODDRE (R&AT) G Singley  
Attn ODDRE (R&AT) S Gontarek  
The Pentagon  
Washington DC 20301-3080

OSD  
Attn OUSD(A&T)/ODDDR&E(R) J Lupo  
Washington DC 20301-7100

CECOM  
Attn PM GPS COL S Young  
FT Monmouth NJ 07703

CECOM RDEC Elect System Div Dir  
Attn J Niemela  
FT Monmouth NJ 07703

CECOM  
Sp & Terrestrial Commctn Div  
Attn AMSEL-RD-ST-MC-M H Soicher  
FT Monmouth NJ 07703-5203

Dir of Assessment and Eval  
Attn SARD-ZD H K Fallin Jr  
103 Army Pentagon Rm 2E673  
Washington DC 20301-0163

Hdqtrs Dept of the Army  
Attn DAMO-FDT D Schmidt  
400 Army Pentagon Rm 3C514  
Washington DC 20301-0460

MICOM RDEC  
Attn AMSMI-RD W C McCorkle  
Redstone Arsenal AL 35898-5240

US Army Avn Rsrch, Dev, & Engrg Ctr  
Attn T L House  
4300 Goodfellow Blvd  
St Louis MO 63120-1798

US Army CECOM Rsrch, Dev, & Engrg  
Attn R F Giordano  
FT Monmouth NJ 07703-5201

US Army Edgewood Rsrch, Dev, & Engrg Ctr  
Attn SCBRD-TD J Vervier  
Aberdeen Proving Ground MD 21010-5423

US Army Info Sys Engrg Cmnd  
Attn ASQB-OTD F Jenia  
FT Huachuca AZ 85613-5300

US Army Materiel Sys Analysis Agency  
Attn AMXSY-D J McCarthy  
Aberdeen Proving Ground MD 21005-5071

US Army Matl Cmnd  
Dpty CG for RDE Hdqtrs  
Attn AMCRD BG Beauchamp  
5001 Eisenhower Ave  
Alexandria VA 22333-0001

US Army Matl Cmnd  
Prin Dpty for Acquisition Hdqtrs  
Attn AMCDCG-A D Adams  
5001 Eisenhower Ave  
Alexandria VA 22333-0001

US Army Matl Cmnd  
Prin Dpty for Techlgy Hdqtrs  
Attn AMCDCG-T M Fisette  
5001 Eisenhower Ave  
Alexandria VA 22333-0001

US Army Mis Cmnd  
Attn AMSMI-RD-HW J Cole  
Attn AMSMI-RD-SS-SE J Jordan  
Redstone Arsenal AL 35898

US Army Natick Rsrch, Dev, & Engrg Ctr  
Acting Techl Dir  
Attn SSCNC-T P Brandler  
Natick MA 01760-5002

## Distribution

US Army Rsrch Ofc  
Attn G Iafrate  
4300 S Miami Blvd  
Research Triangle Park NC 27709

US Army Simulation, Train, & Instrmntn  
Cmnd  
Attn J Stahl  
12350 Research Parkway  
Orlando FL 32826-3726

US Army Tank-Automtv & Armaments Cmnd  
Attn AMSTA-AR-TD C Spinelli  
Bldg 1  
Picatinny Arsenal NJ 07806-5000

US Army Tank-Automtv Cmnd Rsrch, Dev, &  
Engrg Ctr  
Attn AMSTA-TA J Chapin  
Warren MI 48397-5000

US Army Test & Eval Cmnd  
Attn R G Pollard III  
Aberdeen Proving Ground MD 21005-5055

US Army Train & Doctrine Cmnd  
Battle Lab Integration & Techl Dirctr  
Attn ATCD-B J A Klevecz  
FT Monroe VA 23651-5850

US Military Academy  
Dept of Mathematical Sci  
Attn MAJ D Engen  
West Point NY 10996

USAASA  
Attn MOAS-AI W Parron  
9325 Gunston Rd Ste N319  
FT Belvoir VA 22060-5582

Nav Surface Warfare Ctr  
Attn Code B07 J Pennella  
17320 Dahlgren Rd Bldg 1470 Rm 1101  
Dahlgren VA 22448-5100

GPS Joint Prog Ofc Dir  
Attn COL J Clay  
2435 Vela Way Ste 1613  
Los Angeles AFB CA 90245-5500

DARPA  
Attn B Kaspar  
Attn L Stotts  
3701 N Fairfax Dr  
Arlington VA 22203-1714

ARL Electromag Group  
Attn Campus Mail Code F0250 A Tucker  
University of Texas  
Austin TX 78712

Dir for MANPRINT  
Ofc of the Deputy Chief of Staff for Prsnl  
Attn J Hiller  
The Pentagon Rm 2C733  
Washington DC 20301-0300

The Boeing Company  
McDonnell Aircraft & Mis Syst  
Attn J Roedder  
PO Box 516 Mail Code S064226  
ST Louis MO 63166

US Army Rsrch Lab  
Attn AMSRL-SE-RM B Bender  
Attn AMSRL-SE-RM R Tan  
Attn AMSRL-SE-RM S Stratton  
Attn AMSRL-SL-BV G Durfee  
Attn AMSRL-WM-WB D McGee  
Aberdeen Proving Ground MD 21005

US Army Rsrch Lab  
Attn AMSRL-CI-LL Techl Lib (3 copies)  
Attn AMSRL-CS-AL-TA Mail & Records  
Mgmt

Attn AMSRL-CS-AL-TP Techl Pub (3 copies)  
Attn AMSRL-SE-RM B Wallace  
Attn AMSRL-SE-RM D W Vance  
Attn AMSRL-SE-RM E Burke  
Attn AMSRL-SE-RM G Goldman  
(20 copies)  
Attn AMSRL-SE-RM H Dropkin  
Attn AMSRL-SE-RM J Silverstein  
Attn AMSRL-SE-RM J Silvius  
Attn AMSRL-SE-RM P Cremona-Simmons  
Attn AMSRL-SE-RM R Wellman  
Attn AMSRL-SE-RM T Pizzillo

## Distribution

US Army Rsrch Lab (cont'd)  
Attn AMSRL-SE-RS A Sindoris  
Attn AMSRL-SE-RU B Merchant  
Attn AMSRL-SE-RU B Scheiner  
Attn AMSRL-SE-RU J Sinchina

US Army Rsrch Lab (cont'd)  
Attn AMSRL-SE-RU R Innocenti  
Attn AMSRL-SE-RU J McCorkle  
Adelphi MD 20783-1197

REPORT DOCUMENTATION PAGE			Form Approved OMB No. 0704-0188	
Public reporting burden for this collection of information is estimated to average 1 hour per response, including the time for reviewing instructions, searching existing data sources, gathering and maintaining the data needed, and completing and reviewing the collection of information. Send comments regarding this burden estimate or any other aspect of this collection of information, including suggestions for reducing this burden, to Washington Headquarters Services, Directorate for Information Operations and Reports, 1215 Jefferson Davis Highway, Suite 1204, Arlington, VA 22202-4302, and to the Office of Management and Budget, Paperwork Reduction Project (0704-0188), Washington, DC 20503.				
1. AGENCY USE ONLY (Leave blank)		2. REPORT DATE January 1998		3. REPORT TYPE AND DATES COVERED Final, October 1996 to October 1997
4. TITLE AND SUBTITLE RCS Validation of a Missile-Shaped Target at W-Band			5. FUNDING NUMBERS DA PR: AH16 PE: 62120A	
6. AUTHOR(S) Geoffrey H. Goldman				
7. PERFORMING ORGANIZATION NAME(S) AND ADDRESS(ES) U.S. Army Research Laboratory Attn: AMSRL-SE-RM (ggoldman@arl.mil) 2800 Powder Mill Road Adelphi, MD 20783-1197			8. PERFORMING ORGANIZATION REPORT NUMBER ARL-TR-1563	
9. SPONSORING/MONITORING AGENCY NAME(S) AND ADDRESS(ES) U.S. Army Research Laboratory 2800 Powder Mill Road Adelphi, MD 20783-1197			10. SPONSORING/MONITORING AGENCY REPORT NUMBER	
11. SUPPLEMENTARY NOTES AMS code: P622120.H16 ARL PR: 8NE4H1				
12a. DISTRIBUTION/AVAILABILITY STATEMENT Approved for public release; distribution unlimited.			12b. DISTRIBUTION CODE	
13. ABSTRACT (Maximum 200 words)  In a comparison of measured, simulated, and theoretical calculations of radar cross section (RCS), the radar target was a simple missile shape (a cylinder with hemispherical ends). For the measurements, the target was rotated on a turntable from -5° to 365° in azimuth, and its RCS was measured with a W-band frequency-agile instrumentation radar. (Clutter and noise in the measured RCS data were reduced by spatial filtering.) For modeling the target geometry, the ACAD (advanced computer-aided design) geometric modeling program was used to create both an IGES (initial graphics exchange specification) and a facet model. For modeling the RCS, three high-frequency prediction codes were used (Xpatch, CADDSCAT, and NcPTD), as well as a point scatter model. Various methods were used to process and simulate the target returns, depending upon the aspect angle. Agreement between the measured and simulated bandwidth-averaged RCS values depended on the portion of the target that dominated the radar return: agreement was close for radar returns dominated by returns from the hemispherical ends of the target. However, for aspect angles near broadside to the target (for which the cylindrical part of the target dominated the returns), RCS measurements suggested an interaction between the target and the pylons supporting it.				
14. SUBJECT TERMS RCS, ISAR, model			15. NUMBER OF PAGES 42	
			16. PRICE CODE	
17. SECURITY CLASSIFICATION OF REPORT Unclassified	18. SECURITY CLASSIFICATION OF THIS PAGE Unclassified	19. SECURITY CLASSIFICATION OF ABSTRACT Unclassified	20. LIMITATION OF ABSTRACT UL	